Solid Freeform Fabrication 2018: Proceedings of the 29th Annual International Solid Freeform Fabrication Symposium – An Additive Manufacturing Conference
Reviewed Paper

CORRELATIVE BEAM PATH AND PORE DEFECT SPACE ANALYSIS FOR MODULATED POWDER BED LASER FUSION PROCESS

Deniz Sera Ertay*, Henry Ma*, Mihaela Vlasea*

*Multi-Scale Additive Manufacturing Laboratory, Department of Mechanical and Mechatronics Engineering, University of Waterloo, 200 University Ave. Waterloo, ON, N2L 3G1, Canada

Abstract

There are ongoing challenges in achieving full density metal parts via Laser Powder Bed fusion (LPBF). Numerous of studies have shown that the part density depends on the process parameters, the powder characteristics and the process environment conditions. The scan strategy and the interactions of scan paths at discontinuities such as borders, create regions with high probability of pore occurrence. In this work, the complex relation between the defects and the toolpath at border discontinuities is investigated for a print recipe which gives >99.95% solid fraction in the core of the part. Samples are scanned by X-ray Computed Tomography (CT). The pore space was analyzed to extract the pore frequency, size, shape and location with respect to the scan path, border and contour strategies.

Introduction

Additive Manufacturing (AM) technologies offer new avenues for design of complex internal topologies and lightweight structures, and overall freedom in design with enhanced part functionality without the need for specialized tooling [1]. AM can also lower costs by reducing the design-to-fabrication cycle and consolidation of multi-part assemblies [1,2]. There is a breakeven point where the need for high-value, low-volume parts or technology-disruptive designs favor the adoption of AM approaches [3].

Laser Powder Bed fusion (LPBF) is one of the main metal additive manufacturing processes, where a layer of metal powder is spread on the build plate and fused by a laser beam following a scan path through the cross-section area of the layer. In LPBF, the complex interaction between the powder and the energy input often results in porosity, microstructure inhomogeneity, and poor mechanical characteristics [4,5]. There is a detrimental impact of porosity on mechanical performance [5]. Porosity highly depends on the energy input, which is determined by the process parameters such as beam power, beam focus, scan speed, layer thickness etc. Morrow et al. studied the effect of porosity on the microstructure of the part and investigated how it affects the overall part quality [4]. Researchers have developed models, where the defect population and porosity were used as a tool to predict the mechanical properties of the part such as fatigue strength and estimated the part life [5]. As there is a direct impact of density on mechanical properties, it is important to reduce the defect population within the part and make it as dense as possible [6].

The studies in literature have shown that the porosity of the parts highly depends on the energy input to the metal powder. The energy input is determined by several process parameters such as laser power, scan speed and layer thickness. These parameters are dominant in determining the energy input per time in a unite volume. Early studies worked on understanding the relationship between the process parameters and the porosity of the part [7]. It has been shown that a

homogeneous energy input and temperature distribution can improve the density of the part [8]. Process parameters are then optimized to improve the density [9–16]. The pore defects are analyzed statistically depending on their size, frequency, morphology and distribution [17,18]. The different types of defects are grouped in three groups in terms of their generation causes: depression collapse, lateral pores, open and trapped pores [18]. Vast number of studies agree low energy input results in defects as there is not enough energy to melt the metal powder [9,11,14,16]. In a later study Cunningham et al. stated that excessive energy input also causes porosity of the part [12]. This is called keyhole mechanism, where materials can be ejected from the melt pool by applying an excessive energy input. The scan path defines how the energy input is distributed on the metal powder substrate. It plays an important role on the energy density and can also determine if there is an excessive or insufficient energy input to the metal powder [8]. Moreover, different scan strategies have been investigated to see the effect on the density of the part. The studies can be extended by deploying different scan strategies at the core and the skin of the part, and the interaction between these two scan strategies.

In this study, the main goal is to identify the relation between defects and the scan path at the skin of the part, where discontinuities of the exposure points happen in LPBF process. Samples are manufactured by using different scan strategies at the periphery (or border) and using a process recipe, which gives 99.95% solid fraction for Invar-alloy at the core of the part. Samples are scanned by a X-ray Computed Tomography (CT), which is a well-suited equipment for defect space analysis [13]. The defects are analyzed statistically to investigate the pore frequency, size, morphology and the location with respect to the toolpath of the laser. In this study, the group was able to identify skin (or periphery) strategies that improve the overall density by minimizing sub-surface pores. This would enhance the tensile and fatigue properties, as sub-surface defects have a high detrimental impact on part mechanical performance.

Material and Methods

Cylindrical samples are manufactured using Renishaw AM400, which is a LPBF system with a modulated laser. Invar-alloy metal powder is used to manufacture the samples. It is a nickel-iron based alloy known for low coefficient of expansion. It has been used in temperature sensitive applications. The chemical content of the Invar-alloy powder can be seen in Table 1. The particle size distribution of the powder is found using a Retsch Camsizer X2 Optical Particle Size Analyzer with the X-Jet dispersion module. Minimum chord length of the powder particles is measured and averaged. The powder size distribution for Invar-alloy powder can be seen in Table 2.

Table 1. Chemical content of Invar-alloy powder (Wt. %)

	Elements								
	Fe	**Ni**	**Mn**	**C**	**Co**	**Mo**	**Cr**	**P**	**S**
Wt. %	Balance	36.12	0.44	0.01	0.01	0.05	0.12	0.002	0.003

Table 2. Powder size distribution of Invar-alloy

	D10	**D50**	**D90**

Average size of min. x_c (µm)	23.2	33.6	45.0

The samples are 5 mm in diameter and 8 mm in height, specifically designed for ease in density and pore space measurements via CT scanning. The process parameters are optimized to achieve high density at the core of the part. In this study, the core parameters used in manufacturing the samples were kept constant, to isolate the occurrence of defects due to the contribution of parameters sets at the periphery of the parts. The core process parameters used for manufacturing the samples used in this study are summarized in Table 3, with a meander scan strategy, with a 67^{o} meander rotation angle increment between subsequent layers. With these parameters, higher than 99.95% density has been achieved at the core of the samples.

Table 3. Process parameters for the core scan strategy used to manufacture the samples investigated in this study

Laser power	**Exposure time**	**Point distance**	**Hatch distance**	**Layer thickness**
275 W	70 µs	60 µm	60 µm	30 µm

Four different border scan strategies are used to observe the effect on the defect population at the periphery of parts. These strategies are (i) blocked path, (ii) border path, (iii) contour path, shown in Figure 1a and (iv) hatch compensation factor shown in Figure 1b. The blocked path (i) is used to reduce the number of scans in thin areas to a single scan. The border scan path (ii) circumferences the 2D cross-section area of the layer geometry and it is the outermost scan exposure. It is recommended to have a border scan at each layer to improve the surface structure and quality [19]. The contour scan (iii) mimics the border with a certain offset from the border. The contour scan is intended to reduce the porosity between the hatch and the border by re-melting discontinuities. Hatch compensation factor (iv) is a feature of the modulated beam process, where additional points can be added at the end of the hatch lines, if the distance between the last exposure point on a hatch line and the border line is bigger than the user-defined threshold. This distance can be identified as a percentage of the hatch space used in the recipe. The scan strategy and corresponding process parameters used in manufacturing of the part periphery in this study is shown in Table 4. As it is summarized in Table 3, the laser power used at the core of the parts is 275 W. However, the laser power varies at the skin laser scan. The border power sample 11 is the same as core power and the blocked path power is 110 W. The border power the samples 01, 09, 17 and 25 is 250 W and the contour power is set at 50% of the core power. The skin scan re-melts some of the regions. In order to prevent excessive energy input the skin laser power is chosen lower than the core laser power. Additionally, samples with the same periphery scan strategies are printed, but with a core meander rotation angle of 107^{o} and the rest of the parameters the same to see the effect on sub-surface density of the part.

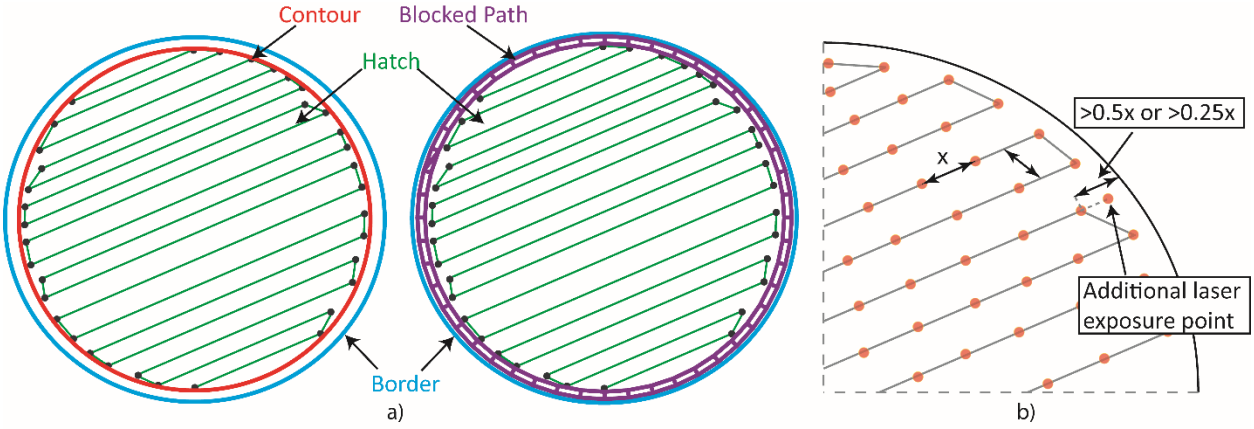

Figure 1. Scan strategies used in this study: a) Border, hatch, contour, blocked path, b) hatch compensation factor

Table 4. Scan strategies of analyzed samples (H: Hatch, B: Border, C: Contour, BP: Blocked path)

		Hatch Compensation		
		0%	25%	50%
Scan Strategy	H+B+C		Sample #01	Sample #09
	H+B		Sample #17	Sample #25
	H+B+BP	Sample #11		

ZEISS Xradia 520 Versa 3D X-ray Nano-CT is used to scan the samples. The CT data give the 3D visualization of the part with the defects. For this scan, the voxel size of 12 μm is used to detect the defects. CT analytics were deployed to extract the coordinates of the defect centroid within each CT scanned surface and in 3D space, which determines the defect location relative to the sample geometry. The location of the defect center at each layer is extracted. The size of the defect cross-section in pixels at each layer is given to have a better understanding of how the defect is seeded, grown up and shrunk. The volumetric fraction is another output of the CT data. It is given as a percentage at each layer. The cross-section size and the volumetric fraction data give a quantified measure of how the defect is seeded, grown up and shrunk. A distinct number is assigned to each individual defect within a part, to keep the track of defects at each layer.

For this analysis the defects at the core of the part are not included, as the amount is negligible compared to the defects occurred at the skin of the part and were optimized in another study. It has been previously observed that for parameter sets optimized in the core, the defects exist where the core scan path discontinuities intersect the skin scan path(s). This means that the process recipe works well for achieving high density parts when the laser exposure points are homogeneously distributed, and that the edges of the part are problematic. In this study, the group was able to identify skin (or periphery) strategies that improve the overall density by minimizing sub-surface pores.

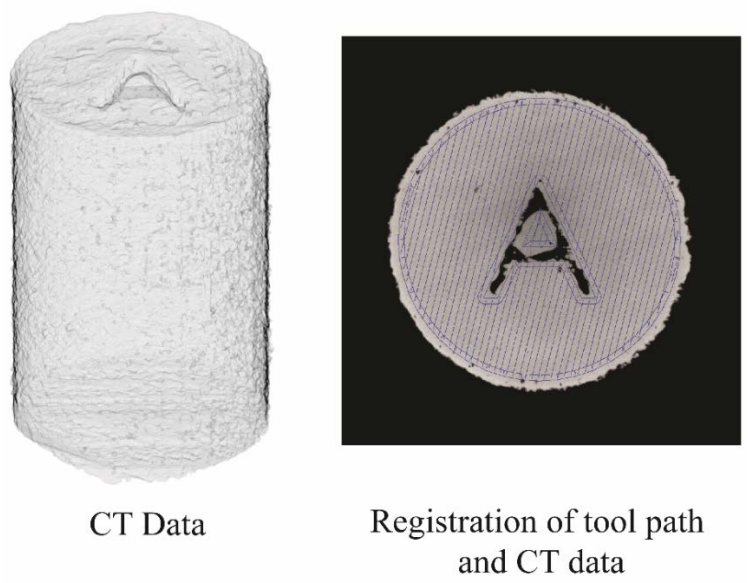

Figure 2. Data registration of CT with the scan path

Distinctive registration markers are printed on top of the samples, shown in Figure 2, to register the CT scan data with the scan path and to help in part identification. Only the laser exposure points at the end of the hatch lines and the skin (border, contour and blocked path) exposure points are extracted from the scan path data as this study is focused on analyzing the defects occurred at the skin of the part. The defect centers at each layer are analyzed together with respect to the near-by laser exposure points.

Statistical Analysis of the Defect Space

The CT scan data was analyzed statistically to determine which skin scan strategy works best for achieving high density parts. In Figure 3, the periphery defect population for all the parts manufactured with different scan strategies are shown. The most defects have been obtained in sample 11, where border and blocked path scan strategies are used at the skin of the part. The reason for that could be excessive number of laser exposure points at the skin of the part. The core meander hatch lines are rotating 67^{o} from one layer to another in all these parts to have an alternating direction of the beam raster direction between layers and avoid compounding layer-by-layer defects resulting from stacking the beam path. On the other hand, the skin exposure points, on border, contour and blocked path, are not rotating and changing position on the x-y plane. They occur at the same position on each layer. It means that the energy is localized on specific points. The stacked laser exposure points contribute to the defects occurring at the skin. Furthermore, the blocked path lines create more discontinuities at the skin of the samples. Although they are homogeneously distributed through the circumference of the sample, they are still causing a discontinuity radially. In this study, only the defects at skin are analyzed, where the skin is 0.2 mm deep from the actual part border radially.

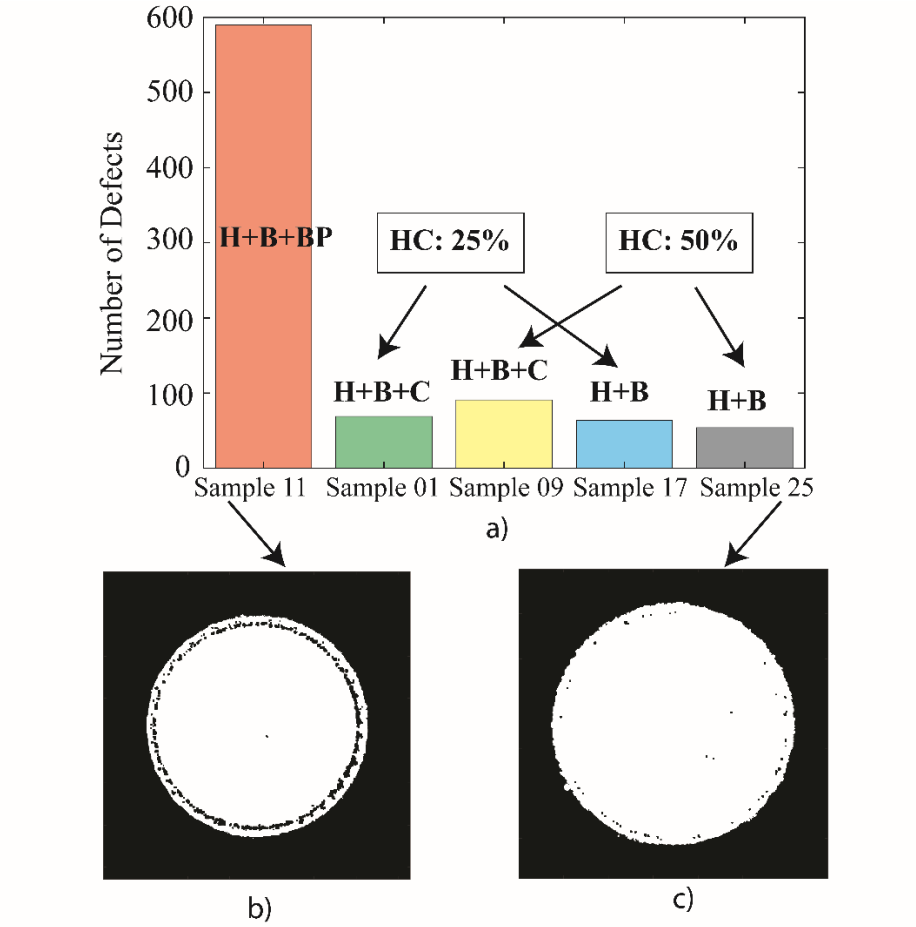

Figure 3. a) Defect population in different samples, where H, B, C, BP and HC represent hatch, border, contour, blocked path and hatch compensation, respectively, b) the flattened CT images of the cylindrical part (sample 11) black spots show the defects, c) the flattened CT images of the cylindrical part (sample 25) black spots show the

The histogram of defect population in different samples can be seen in Figure 3. There is an approximately 84% reduction of defect population on the skin of the part, when the blocked path scan strategy is muted. The other four parts show a similar range of defects at the skin. The best performance is observed, when only border strategy is used on the skin and 50% hatch compensation is enabled. An in-depth discussion is provided by analyzing the population of defects in detail in terms of pore size and depth.

The depth of the defects is analyzed statistically for each part. The depth is quantified as the number of process layers over which a pore defect exists. Depth of two means that the defect propagates through two layers of the process, where the layer thickness is 30 µm for this process recipe. The Figure 4 shows the histogram of the defect population grouped according to their depth. It can be seen that each part shows the same trend in the histograms. Most of the defects propagate through 2 and 3 layers in each part. In general, there are only a few defects, which propagates through more than 5 layers or less than 2 layers. The depth can give an idea about the cause of the defect. In literature it has been stated that shallow defects with irregular shape are caused by poorly chosen process parameters, where the energy input is not enough and the process is under-melting [17]. The shallow defects occurring in less than one-layer thickness are usually caused by

entrapped gas. The depth of the defect can also change during manufacturing of the part. If a defect occurs due to lack of energy, this can be compensated by the laser exposure points on the next layer. So that the next layer can play a corrective role for the previous layer.

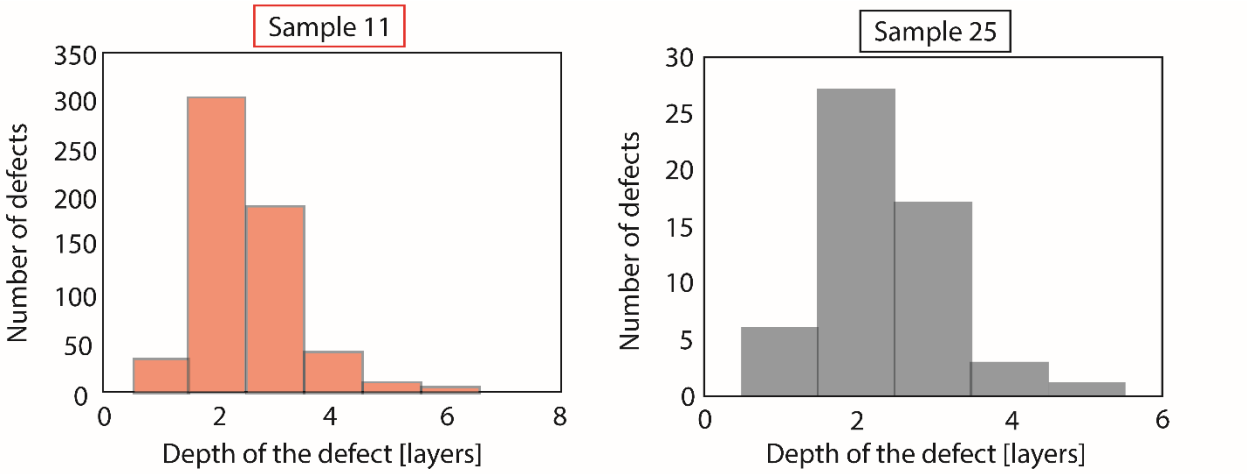

Figure 4. Histogram of the defect depth at the skin, given in number of layers. It shows the depth distribution of the defects within one part.

The morphology of the defects is analyzed statistically. It can be also an indicator of the defect initiator. In this analysis, the biggest volumetric fraction of the defect is located within the defect layers. If there is a defect with 4 layers in depth and the biggest volume of the defect occurs in the second layer, it means that the biggest volumetric fraction is at the second layer of the defect from the bottom. The defects are grouped according to their depth. Figure 5 shows the histograms of the biggest volumetric fraction location within the defect for each depth of the defect. It is observed that the biggest volumetric fraction usually occurred in the middle layers of the defect. It means that the defect is seeded first, it grows up and then shrinks during the manufacturing of the part. For defects which span multiple layers, the largest circumference of the defect occurred in layers 2 and 3. For instance, in Sample 25, defects span up to 5 layers; for example, for the population of defects spanning 4 layers Figure 5 (25-c), the largest segment in most pores occurred in the second layer.

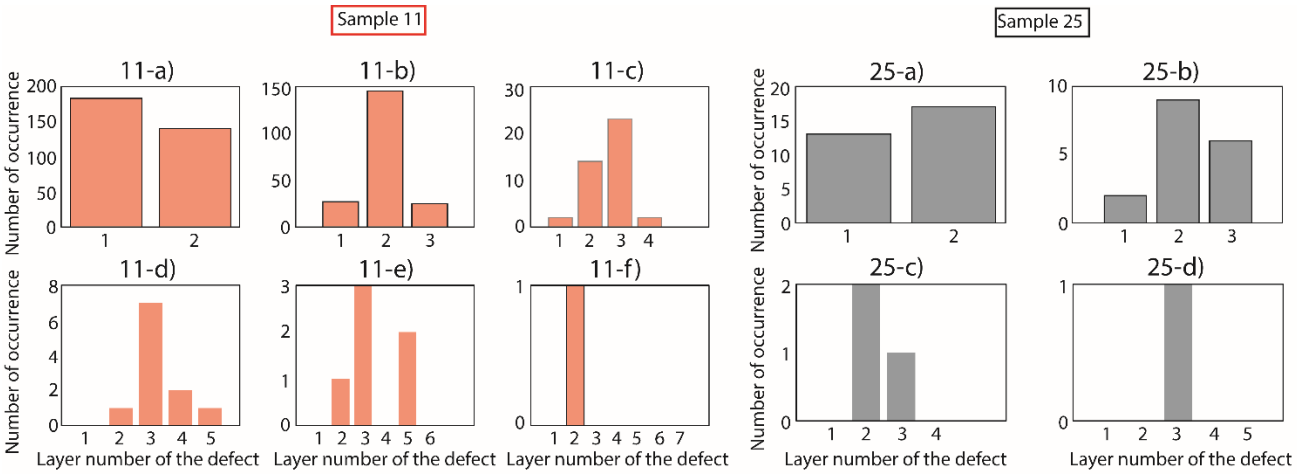

Figure 5. For most defects which span multiple layers, the histogram showcases the frequency of the layer where the biggest pore volume exists. The layer is indicated, where the biggest volumetric fraction of the defect happens.

In the case of the samples studied, one of the main causes for a defect is lack of fusion. It is observed that there are less exposure points on the skin of the samples at specific locations, depending on the orientation of the hatch lines in relationship to the skin scan strategies. In order to determine these locations analytically, the position of the laser exposure points and the defect is transferred to polar coordinates. The angle between the laser exposure point normal to the surface of the sample and the hatch lines are calculated. This angle is called α shown in Figure 6. When this angle gets closer to 90^{o}, the distance between the laser exposure points at the end of the hatch lines increases, with less laser exposure points per unit area at these specific regions. At the regions, where this angle gets closer to 0^{o}, the population of the laser exposure points increases. Hence, the distance between the laser exposure points gets closer to the distance between the hatch lines.

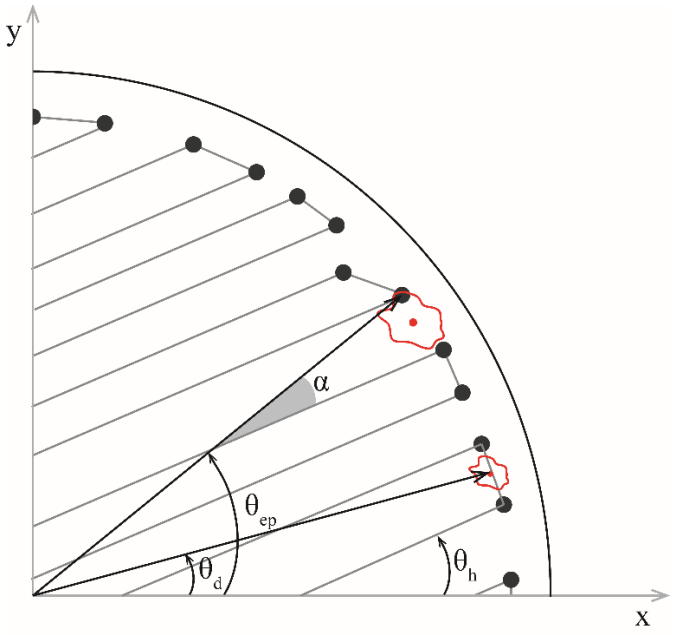

Figure 6. Angular positions of the defects, laser exposure points are shown in θ_d and θ_{ep}. The hatch angle is shown in θ_h with respect to the x-axis. The angle between laser exposure points' angular position and the hatch angle is represented by α.

The defects are investigated layer-by-layer with respect to the scan path of the laser and the laser exposure points. Figure 7 shows the hatch lines in purple, the skin scan path in dark blue and the actual border of the part in pink. The circles show the defect location at each layer and the red circle is used to highlight the biggest volumetric fraction of the defect. It can be seen that the laser exposure points are getting further away from each other when the angle between the laser exposure point normal and the hatch lines is almost perpendicular. This effect can be better observed in Figure 7 on image 25-a) and 11-c).

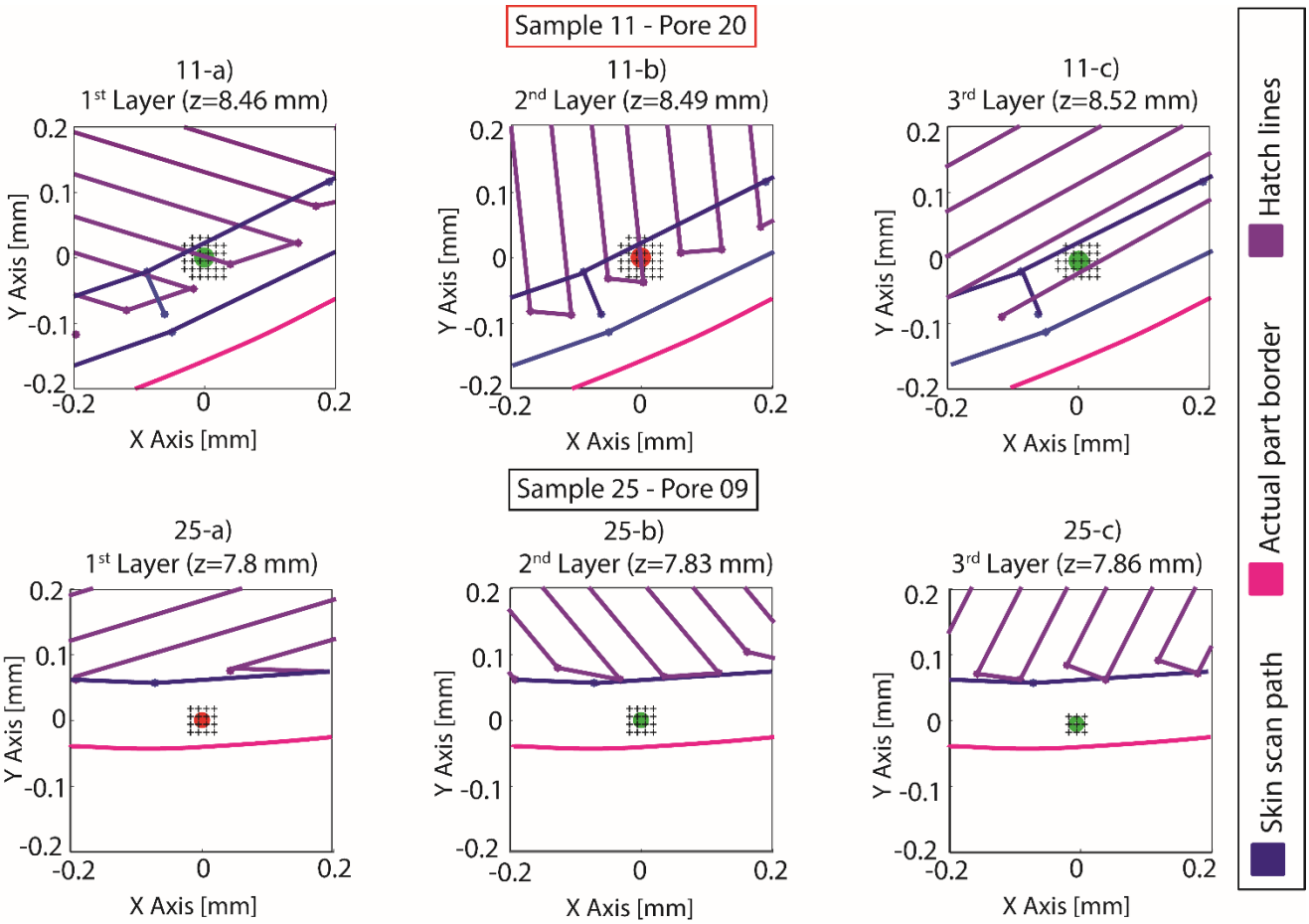

Figure 7. Randomly selected defects with 3 layers in depth from sample 11 and 25 and the scan path on these layers are plotted together. The red and green dots show the centroid of the defect. Red color indicates the biggest volumetric fraction of the defect.

An additional set of experiments was planned to see the effect of the rotation angle of the core meander hatch lines on the defect population at the border. The samples are manufactured with the same processing parameters and the hatch rotation angle is set to 107°. The defect population at the skin of the samples decreased by 20% as shown in Table 5. A random region is observed throughout the layers of the sample 11 and 25. It can be seen that the density of the laser exposure points is changing frequently. For instance, if the density of the laser exposure points is low in one layer, it will be higher on the next layer. This is a result of the rotation angle in this set of experiment being closer to 90° than the first set of experiment. Hence, the layer on top with more laser exposure points is a corrective action to the previous layer. It compensates the lack of energy on the previous layer.

Table 5. Comparison of defect population between two different experiment sets with different hatch rotation angles 67° and 107°

	Defect Population (Number of Defects)			
Hatch rotation angle	**Sample 01**	**Sample 09**	**Sample 17**	**Sample 25**
67°	69	91	64	54
107°	56	60	50	38

It is already observed that the distribution of the laser exposure points is not homogeneous at the skin of the part. In order to see the effect of the density of the laser exposure points on the defect population at the border, the cylindrical samples are sliced, and each slice is investigated throughout the sample at each layer shown in Figure 8. For each slice at each layer, the hatch end points are counted, and that slice is flagged if there is a defect located. With this analysis, it is aimed to develop algorithms to predict defects using a probability distribution function, when a certain set of laser exposure points occur in consecutive layers using statistical and machine learning algorithms. This is part of a work in progress and will be presented as part of published work.

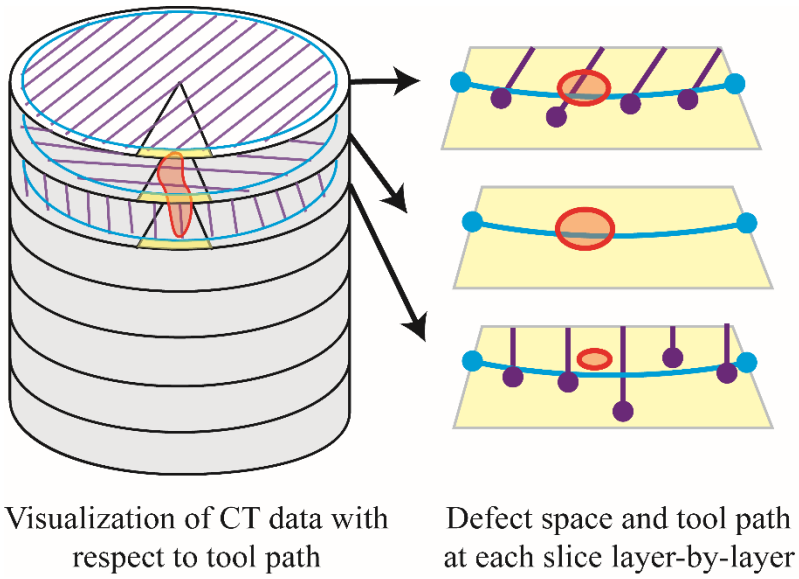

Figure 8. Investigation of laser exposure points and defects at each slice layer-by-layer

Conclusion

In this study, the defects at the skin of the samples are statistically analyzed according to their size, distribution, depth and frequency on samples printed with the same process parameters in the core and different scan strategies at the skin. The statistics of defects in different samples are observed to understand the complex relation between the scan path and the defect occurrence. It is seen that the size distribution of the defects has a very similar trend in every sample although they are printed with different scan strategies. This means that the size distribution and frequency do not change according to the scan strategy. It only dampens the amount of the defects occurred in one sample. The same behavior is also detected in the morphology of the defects, where the defect grows up and shrinks down volumetrically through the longitudinal direction. For future research directions,

a statistical or machine learning tool will be designed to predict the probability of the defect occurrence for a given scan path and strategy. So that possible defects can be detected and avoided by modifying the scan path before manufacturing the parts. This tool will also help to increase the density of the parts especially at the discontinuities of the scan lines (skin of the part) manufactured by LPBF process.

Acknowledgements

This work was supported by funding from the Federal Economic Development Agency for Sothern Ontario (FedDev Ontario), in partnership with our industry partner Burloak Technologies. We would like to acknowledge the contribution of Adeola (Addy) Olubamiji, Material Scientist / Additive Manufacturing Engineer, Burloak Technologies for her support and mentorship throughout the design of experiment, supporting the manufacturing aspect of this work, and for providing valuable technical feedback.

References

[1] Ronald Berger Strategy Consultants, Additive Manufacturing - A game changer for the manufacturing industry?, (2013). http://www.rolandberger.com/media/pdf/Roland_Berger_Additive_Manufacturing_20131129.pdf.

[2] Wohlers Associates, 3D Printing and Additive Manufacturing State of the Industry Annul Worldwide Progress Report, Wohlers Associates, 2017.

[3] S. Merkt, C. Hinke, H. Schleifenbaum, H. Voswinckel, Geometric complexity analysis in an integrative technology evaluation model (ITEM) for selective laser melting (SLM), South Afr. J. Ind. Eng. 23 (2012) 97–105. doi:10.7166/23-2-333.

[4] B.M. Morrow, T.J. Lienert, C.M. Knapp, J.O. Sutton, M.J. Brand, R.M. Pacheco, V. Livescu, J.S. Carpenter, G.T. Gray, Impact of Defects in Powder Feedstock Materials on Microstructure of 304L and 316L Stainless Steel Produced by Additive Manufacturing, Metall. Mater. Trans. A. (2018). doi:10.1007/s11661-018-4661-9.

[5] S. Romano, A. Brückner-Foit, A. Brandão, J. Gumpinger, T. Ghidini, S. Beretta, Fatigue properties of AlSi10Mg obtained by additive manufacturing: Defect-based modelling and prediction of fatigue strength, Eng. Fract. Mech. 187 (2018) 165–189. doi:10.1016/j.engfracmech.2017.11.002.

[6] G. Vastola, Q.X. Pei, Y.-W. Zhang, Predictive model for porosity in powder-bed fusion additive manufacturing at high beam energy regime, Addit. Manuf. (2018). doi:10.1016/j.addma.2018.05.042.

[7] W.E. Frazier, Metal Additive Manufacturing: A Review, J. Mater. Eng. Perform. 23 (2014) 1917–1928. doi:10.1007/s11665-014-0958-z.

[8] V.E. Beal, P. Erasenthiran, N. Hopkinson, P. Dickens, C.H. Ahrens, Scanning strategies and spacing effect on laser fusion of H13 tool steel powder using high power Nd:YAG pulsed laser, Int. J. Prod. Res. 46 (2008) 217–232. doi:10.1080/00207540500168279.

[9] G. Kasperovich, J. Haubrich, J. Gussone, G. Requena, Correlation between porosity and processing parameters in TiAl6V4 produced by selective laser melting, Mater. Des. 105 (2016) 160–170. doi:10.1016/j.matdes.2016.05.070.

[10] S. Yusuf, Y. Chen, R. Boardman, S. Yang, N. Gao, Investigation on Porosity and Microhardness of 316L Stainless Steel Fabricated by Selective Laser Melting, Metals. 7 (2017) 64. doi:10.3390/met7020064.

[11] E. Abele, H.A. Stoffregen, M. Kniepkamp, S. Lang, M. Hampe, Selective laser melting for manufacturing of thin-walled porous elements, J. Mater. Process. Technol. 215 (2015) 114–122. doi:10.1016/j.jmatprotec.2014.07.017.
[12] R. Cunningham, S.P. Narra, C. Montgomery, J. Beuth, A.D. Rollett, Synchrotron-Based X-ray Microtomography Characterization of the Effect of Processing Variables on Porosity Formation in Laser Power-Bed Additive Manufacturing of Ti-6Al-4V, JOM. 69 (2017) 479–484. doi:10.1007/s11837-016-2234-1.
[13] A. Thompson, I. Maskery, R.K. Leach, X-ray computed tomography for additive manufacturing: a review, Meas. Sci. Technol. 27 (2016) 072001. doi:10.1088/0957-0233/27/7/072001.
[14] S. Tammas-Williams, H. Zhao, F. Léonard, F. Derguti, I. Todd, P.B. Prangnell, XCT analysis of the influence of melt strategies on defect population in Ti–6Al–4V components manufactured by Selective Electron Beam Melting, Mater. Charact. 102 (2015) 47–61. doi:10.1016/j.matchar.2015.02.008.
[15] G. Ziółkowski, E. Chlebus, P. Szymczyk, J. Kurzac, Application of X-ray CT method for discontinuity and porosity detection in 316L stainless steel parts produced with SLM technology, Arch. Civ. Mech. Eng. 14 (2014) 608–614. doi:10.1016/j.acme.2014.02.003.
[16] C. Kamath, B. El-dasher, G.F. Gallegos, W.E. King, A. Sisto, Density of Additively-Manufactured, 316L SS Parts Using Laser Powder-Bed Fusion at Powers Up to 400W, 2013. doi:10.2172/1116929.
[17] S. Romano, A. Brandão, J. Gumpinger, M. Gschweitl, S. Beretta, Qualification of AM parts: Extreme value statistics applied to tomographic measurements, Mater. Des. 131 (2017) 32–48. doi:10.1016/j.matdes.2017.05.091.
[18] S.A. Khairallah, A.T. Anderson, A. Rubenchik, W.E. King, Laser powder-bed fusion additive manufacturing: Physics of complex melt flow and formation mechanisms of pores, spatter, and denudation zones, Acta Mater. 108 (2016) 36–45. doi:10.1016/j.actamat.2016.02.014.
[19] L. Parry, I.A. Ashcroft, R.D. Wildman, Understanding the effect of laser scan strategy on residual stress in selective laser melting through thermo-mechanical simulation, Addit. Manuf. 12 (2016) 1–15. doi:10.1016/j.addma.2016.05.014.